

Cite this: *Energy Environ. Sci.*,
2025, 18, 4883

Optimization of crystallization dynamics in wide-bandgap bromine–iodine perovskite films for high-performance perovskite–organic tandem solar cells†

Zonglong Song,[‡] Jiangfeng Wang,[‡] Yuqi Bao,^a Jie Zeng,^a Deng Wang,^a Jiang He,^a Peide Zhu,^a Bo Jiang,^a Zhixin Liu,^a Siru He,^a Yanna Hou,^g Ziyang Hu,^{id}^g Chen Xie,^{id}^h Yongsheng Chen,^{id}^f Yongsheng Liu,^{id}^{*ef} Xingzhu Wang^{*abcd} and Baomin Xu^{id}^{*ab}

The development of efficient and stable wide-bandgap (WBG) bromine–iodine halide perovskites (Br > 20%) is crucial for enhancing the performance of tandem solar cells. Nonetheless, phase separation of I–Br in WBG perovskites under illumination and heating significantly hinders the advancement of tandem devices. This phenomenon is primarily attributed to the uneven spatial distribution of halide ions in WBG films. Moroxydine hydrochloride was introduced into 1.85 eV I–Br mixed WBG perovskite films, effectively optimizing the crystallization dynamics of the perovskite and improving the film stability. Through this approach, a 1.85 eV WBG perovskite solar cell (PSC) was successfully fabricated, achieving a power conversion efficiency (PCE) of 18.76%, an open-circuit voltage (V_{OC}) of 1.387 V, and remarkable operational stability. When applied to perovskite–organic tandem solar cells, this method led to devices with a PCE of 25.98% and a V_{OC} of 2.210 V, setting a new record for the highest V_{OC} reported to date.

Received 15th January 2025,
Accepted 31st March 2025

DOI: 10.1039/d5ee00264h

rsc.li/ees

Broader context

Organic–inorganic metal halide perovskites have revolutionized the field of photovoltaics due to their unique optoelectronic properties, making them a cornerstone of next-generation solar energy technologies. With their tunable bandgap and outstanding power conversion efficiencies (PCEs), perovskites have emerged as a key contender in both single-junction and tandem solar cell architectures. However, challenges such as phase separation, halide migration, and stability issues hinder the realization of high-performance wide-bandgap (WBG) perovskite devices, which are critical for efficient tandem configurations. Recent advances in additive engineering, defect passivation, and interface optimization have shown promise in addressing these issues, enabling improved crystallization and operational stability. In this research, the incorporation of novel additives like moroxydine hydrochloride represents a significant leap forward, offering precise control over crystallization dynamics and facilitating the fabrication of high-quality WBG films. Such innovations not only enhance the PCE and voltage of tandem solar cells but also provide a clearer understanding of the fundamental mechanisms governing perovskite material behavior, paving the way for commercially viable, stable, and efficient photovoltaic solutions.

^a Department of Materials Science and Engineering, Southern University of Science and Technology, Shenzhen, 518055, China^b Department of Materials Science and Engineering, Shenzhen Engineering Research and Development Center for Flexible Solar Cells, and SUSTech Energy Institute for Carbon Neutrality, Southern University of Science and Technology, Shenzhen, 518055, China. E-mail: xubm@sustech.edu.cn^c Shenzhen Putai Technology Co., Ltd, Shenzhen, 518110, China. E-mail: wangxz@sustech.edu.cn^d School of Electrical Engineering, University of South China, Hengyang, 421001, China^e The Centre of Nanoscale Science and Technology and Key Laboratory of Functional Polymer Materials, Institute of Polymer Chemistry, College of Chemistry and Renewable Energy Conversion and Storage Center (RECAST), Nankai University, Tianjin, 300071, China^f The Centre of Nanoscale Science and Technology and Key Laboratory of Functional Polymer Materials, Institute of Polymer Chemistry, College of Chemistry and Renewable Energy Conversion and Storage Center (RECAST), Nankai University, Tianjin, 300071, China. E-mail: liuys@nankai.edu.cn^g Department of Microelectronic Science and Engineering, School of Physical Science and Technology, Ningbo University, Ningbo, 315211, China^h College of New Materials and New Energies, Shenzhen Technology University, Shenzhen, 518118, China† Electronic supplementary information (ESI) available. See DOI: <https://doi.org/10.1039/d5ee00264h>

‡ Z. S. and J. W. contributed equally to this work.

Introduction

Organic–inorganic metal halide perovskites have garnered significant research interest due to their exceptional optoelectronic properties, including tunable optical bandgaps, bipolar carrier transport, low exciton binding energy, high extinction coefficients, long carrier lifetimes, and high mobility.^{1–5} Over the past few decades, perovskite solar cells (PSCs) have shown remarkable progress in power conversion efficiency (PCE), establishing themselves as one of the most promising solution-processed thin-film photovoltaic technologies. The certified PCE in National Renewable Energy Laboratory (NREL) of single-junction PSCs has notably increased to 26.7% in 2024.^{6,7} However, the theoretical efficiency of single-junction PSCs is limited to 33.7% due to the Shockley–Queisser (S–Q) radiative limit.⁸ To overcome this bottleneck, the development of perovskite tandem solar cells is essential.⁹ Perovskite photovoltaic materials, with a tunable bandgap range of 1.2–3.0 eV, can be integrated with narrow-bandgap perovskites, silicon solar cells, or organic solar cells to form tandem devices and are widely regarded as one of the most commercially promising photovoltaic technologies.^{10–15}

The bandgap (E_g) of perovskite materials can be tuned by adjusting the ratio of halide ions (iodide and bromide) in the precursor solution. However, when the bromine (Br) concentration exceeds 20%, the crystallization process of wide-bandgap (WBG) perovskite films becomes significantly more complex, hindering the formation of high-quality WBG films.¹⁶ Additionally, stability challenges significantly restrict the applicability of WBG perovskites in tandem devices.¹⁷

On the one hand, studies have demonstrated that iodide (I) and Br exhibit significantly different crystallization rates during the formation of perovskites.¹⁸ Br[−], due to its smaller ionic radius, nucleates more readily, leading to a faster crystallization rate. This disparity in crystallization kinetics results in uneven vertical halide distribution, ultimately causing phase separation within the WBG perovskite film.^{19,20} Secondly, WBG perovskites are susceptible to halide ion migration because halide ions (e.g., Br[−] and I[−]) have a low migration activation energy within the crystal structure.^{21,22} Under illumination or elevated temperatures, halide ions redistribute, forming Br-rich and I-rich regions.²³ Br-rich and I-rich regions can chemically interact with film interfaces or defects, causing material degradation.²⁴ Additionally, WBG perovskites exhibit a high density of lattice defects, including halide vacancies and anti-site defects, which promote non-radiative recombination and accelerate material degradation. These defects also create pathways for halide ion migration, further undermining the stability of films and devices.²⁵ Developing high-performance and stable perovskite tandem devices requires overcoming the challenges associated with WBG materials.

Significant improvements in the efficiency and operational stability of WBG perovskites have been achieved through additive engineering, defect passivation, interface optimization, and encapsulation techniques. The introduction of functional additives (MAI, Pb(SCN)₂ or RbI) has been shown to regulate crystallization kinetics, adjusting nucleation and

growth rates to improve crystal quality and suppress phase separation.^{8,26,27} To achieve high-quality WBG films, researchers have optimized the perovskite crystallization process by refining the solvent system. For instance, the use of a dimethyl sulfoxide (DMSO) and *N,N*-dimethylformamide (DMF) mixed solvent enhances the complexation balance between I and Br ions, promoting uniform nucleation and crystal growth. This approach effectively controls crystallization rates and prevents vertical chemical distribution imbalances, resulting in improved WBG film quality and device performance.²⁸ Functional molecules (aminoethane sulfonic acid) can effectively passivate surface and bulk defects through their amino and sulfonic groups, reducing the trap density and ion migration activity.²⁹ In terms of interface modification, introducing 2D perovskites (PEA⁺ modification) on WBG perovskite surfaces forms passivation layers, effectively preventing ion migration.³⁰

Despite significant advancements in WBG device performance, achieving highly stable WBG perovskites with a bandgap greater than 1.8 eV and low voltage deficits remains a substantial challenge. Therefore, a comprehensive strategy is urgently needed to better understand the crystallization dynamics and vertical distribution characteristics of WBG perovskite films.

Here, we incorporate Moroxydine Hydrochloride (MODCl) into 1.85 eV WBG perovskites, targeting to optimize the crystallization process of WBG films and facilitating the formation of high-quality WBG perovskite films. MODCl strongly interacts with the lead and halide ions in perovskites, optimizing the crystallization dynamics and improving the crystallization quality of WBG films, thereby suppressing phase separation. *In situ* steady-state fluorescence revealed the dynamic evolution of the WBG perovskite crystallization process, while transient absorption measurements further validated the effectiveness of this strategy. Using this method, we successfully fabricated a 1.85 eV WBG PSC with a power conversion efficiency (PCE) exceeding 18.76%, an open-circuit voltage (V_{OC}) of 1.387 V, and excellent operational stability. This method resulted in a PCE of 25.98% and an impressive V_{OC} of 2.210 V in perovskite–organic tandem solar cells (P–OTSCs), establishing a new record for the highest V_{OC} ever reported. It provides valuable insights into the crystallization kinetics of mixed halide perovskites, presenting a straightforward and efficient method for fabricating high-performance WBG PSCs and P–OTSCs.

Results and discussion

Perovskite films and devices were prepared using a one-step spin-coating method (Fig. 1a), with a device architecture of FTO/4PACB/WBG/C60/BCP/Cu. The chemical structure of the MODCl molecule is presented in Fig. S1 (ESI[†]). For clarity, the perovskite precursor solution containing MODCl is hereafter referred to as “target”. To investigate the impact of the concentration of MODCl on device performance, we introduced MODCl of different concentrations (0.1, 0.3 and 0.5 mol%) into the perovskite precursor solution. As shown in Table S1 (ESI[†]),

the device with 0.3 mol% MODCl achieved the best performance. The electrostatic potentials of MODCl were calculated *via* density functional theory (DFT), as illustrated in Fig. 1b. The MODCl molecule exhibits an electron-rich region (red area) concentrated around the C–O–C and C=N groups, suggesting that these electron-rich groups effectively passivate Pb²⁺ defects.³¹ Proton nuclear magnetic resonance (¹H NMR) analysis was conducted on solutions containing MODCl with FAI or PbI₂. As shown in Fig. 1c, the H atom adjacent to the O atom in MODCl exhibited an upfield chemical shift, indicating coordination between MODCl and Pb²⁺ *via* the O atom. Additionally, a downfield shift of the NH₃⁺ group in MODCl was observed, primarily attributed to the hydrogen bonding interactions between MODCl and halide ions. This interaction increases the electron density, thereby enhancing the shielding effect.³² Fig. 1d demonstrates a similar trend, further confirming the interaction between MODCl and FAI. Fourier transform infrared (FTIR) spectra were investigated to study the interactions between MODCl and perovskites (Fig. 1e and Fig. S2, ESI[†]). Upon addition of MODCl, the C=N stretching peak in FA⁺ shifted from 1715.73 cm⁻¹ to 1713.77 cm⁻¹, suggesting that MODCl formed a hydrogen bond with FAI. The asymmetric and symmetric stretching vibrations of the C–O–C bonds in the control WBG film appeared at 1046.85 cm⁻¹ and 1013.33 cm⁻¹, respectively. In the target film, these peaks shifted to

1050.61 cm⁻¹ and 1016.41 cm⁻¹. These shifts indicate the formation of ligand bonds or other interactions between MODCl and PbI₂.

The chemical states of the surface elements in WBG films were analyzed using X-ray photoelectron spectroscopy (XPS). As shown in Fig. 1f, the target WBG film showed two prominent I 3d peaks at 619.32 eV (I 3d_{5/2}) and 630.82 eV (I 3d_{3/2}). In the control WBG films, the I 3d_{5/2} peak appeared at 619.57 eV. Compared to the control film, the I 3d peaks in the target film shift to lower binding energies. A similar trend was seen in the binding energy shifts of the Pb 4f and N 1s peaks, as shown in Fig. 1g and h. These results demonstrate that the chemistry of Pb²⁺ and I⁻ targeting to optimize in WBG films was altered by the introduction of the MODCl additive, as evidenced in the XPS measurements.

In order to explore the influences of MODCl additives on the WBG film morphology, we utilized scanning electron microscopy (SEM) to characterize the morphological changes before and after doping. As shown in Fig. 2a and b, the target WBG film exhibited significantly larger grains (~500–600 μm) and reduced PbI₂ residues, as well as consistent substrate-to-surface grain growth, favoring efficient carrier transport to the electrodes.³³ As depicted in Fig. S3 (ESI[†]), the cross-sectional SEM images of the target films indicate vertically aligned crystal structures with significantly reduced grain boundaries compared

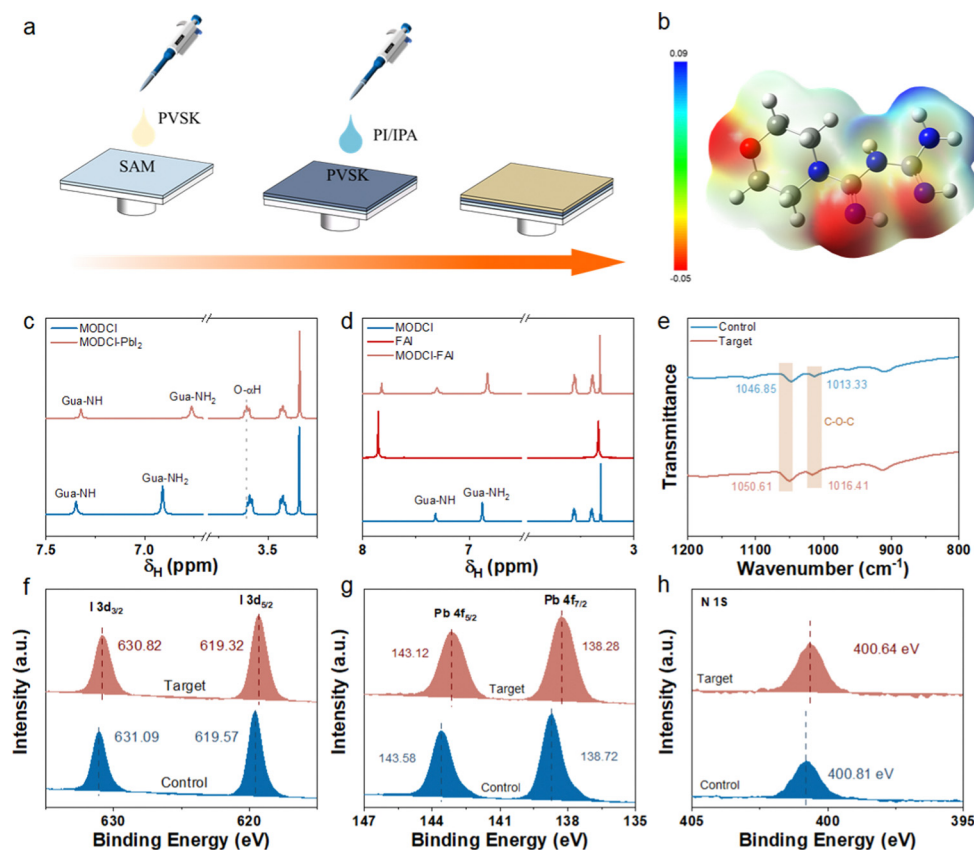


Fig. 1 (a) Process diagram of a one-step spin-coating method of preparing WBG films. (b) The calculated electrostatic potentials of MOD. The color bars from red to blue signal an increase of electropositivity. (c) and (d) Chemical shift information of the MODCl and MODCl (FAI or PbI₂) complex obtained from ¹H NMR measurements. (e) FTIR spectral patterns of the control and target. (f)–(h) XPS spectra of the control and target WBG films.

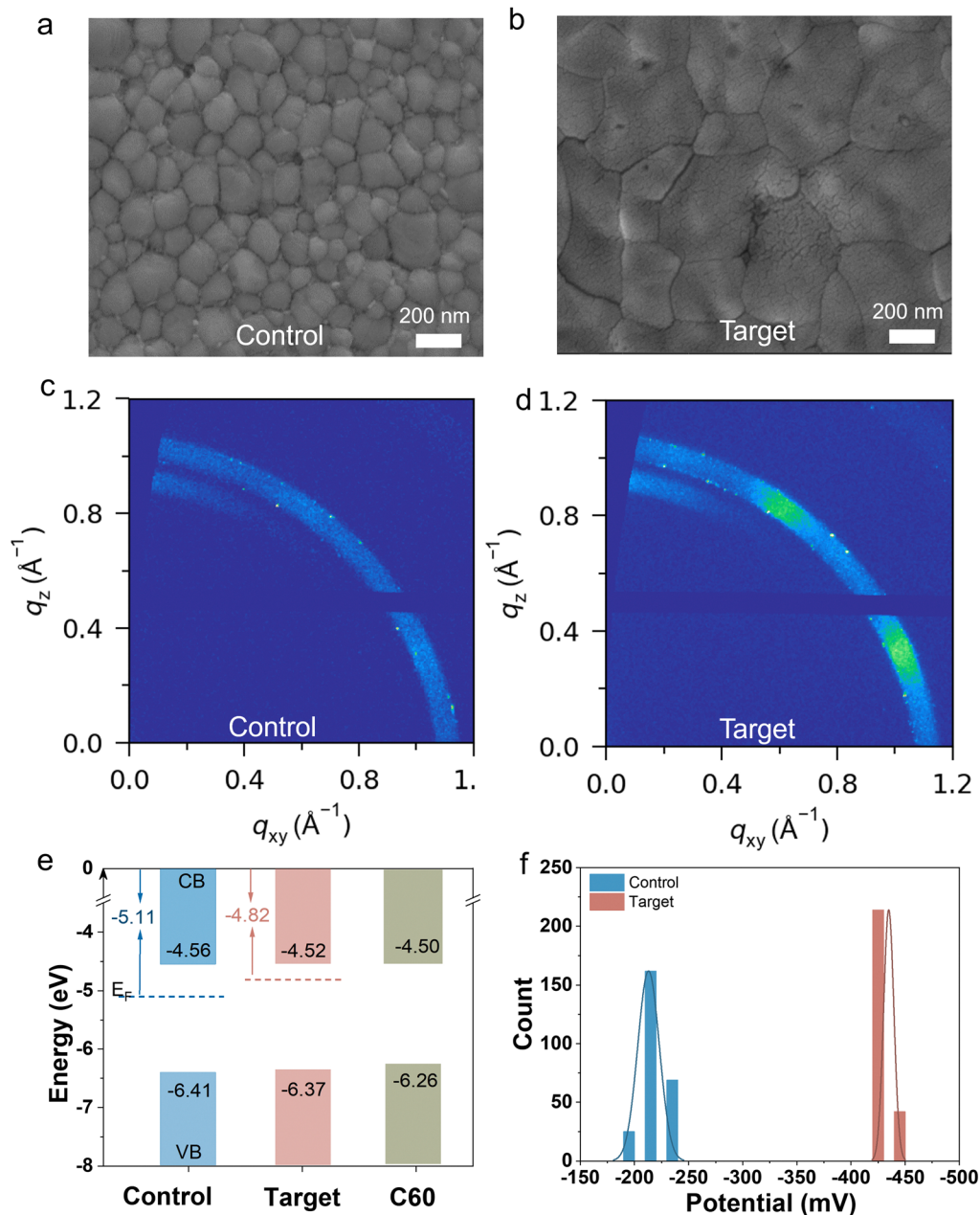


Fig. 2 (a) and (b) SEM images of the control and target WBG films. (c) and (d) The GIWAXS images of the control and target WBG films. (e) Energy-level diagrams of the control and target WBG films. (f) The KPFM images of the control and target WBG films.

to that of the control films, effectively lowering the defect density.⁴ In addition to the excellent WBG film morphology, the target films showed a significant increase in crystallinity (Fig. S4, ESI[†]). X-ray powder diffraction (XRD) patterns further supported the observed reduction of PbI_2 sheets in the SEM images, suggesting that MODCl interacts with the unliganded Pb^{2+} , thereby regulating film growth to form fully developed grains. Atomic force microscopy (AFM) measurements further confirmed the dramatic improvement in the crystal quality of the target WBG films (Fig. S5, ESI[†]). The root-mean-square roughness of the WBG films decreased from 8.9 nm (control film) to 5.1 nm (target film), respectively. Reducing the roughness of perovskite

films can minimize carrier recombination, thereby effectively enhancing the open-circuit voltage (V_{OC}).³⁴ Furthermore, a smooth film surface can effectively reduce light scattering, enhance light harvesting efficiency, and consequently increase the photocurrent density.³⁵ Grazing incidence wide angle X-ray scattering (GIWAXS) was employed for the purpose of characterizing changes in the crystallinity of WBG films after the introduction of MODCl. As shown in Fig. 2c and d, the intensity of the target WBG film (110) diffraction peak increased dramatically, and the diffraction pattern transitioned from a diffuse ring to distinct spot features. These changes clearly indicate a significant improvement in the film's crystallinity, providing

strong structural support for enhancing the optoelectronic performance of the film.³⁶

As shown as Fig. S6 (ESI[†]), the WBG film with MODCl exhibits an optical bandgap (E_g) of 1.854 eV, which is somewhat higher than that of the control WBG film ($E_g = 1.848$ eV). Fig. 2e and Fig. S6 (ESI[†]) display the energy level diagrams for the control and target WBG films, respectively. After introducing MODCl, the secondary electron cutoff (E_{cutoff}) changed to a higher binding energy, demonstrating that MODCl reduces the Fermi level (E_F) of the perovskite films (Fig. S7, ESI[†]). Notably, the valence band maximum (VBM) of the target film exhibits a larger energy gap, suggesting that the target perovskite film is more n-type.³⁷ The target film's VBM was closer to the CBM of C60 at the n-type contact, promoting improved charge transfer at the C60 electron-selective layer and the WBG film interface. The surface potential images obtained *via* Kelvin probe force microscopy (KPFM) (Fig. 2f and Fig. S8, ESI[†]) showed that the potential of the WBG film with MODCl significantly decreases and its distribution narrows compared to that of the control film. The potential range of the WBG film with MODCl

(−440 mV) was considerably lower than that of the control film (−220 mV), demonstrating more prominent n-type characteristics consistent with UPS measurements.

Employing grazing incidence XRD, the impact of MODCl on the residual strain of WBG films was examined. Fig. S9 (ESI[†]) displays the comprehensive XRD patterns and linear fitting of $2\theta - \sin^2\psi$. Tensile strain perpendicular to the film's plane was shown by the fitted curve's positive slope. After introducing MODCl, the tensile strain in the perovskite film was transformed into compressive strain, and residual stress was alleviated, indicating that MODCl effectively mitigates residual strain and contributes to the stability of the perovskite lattice.³⁸

To further investigate the crystallization dynamics of WBG films, we employed *in situ* photoluminescence (PL) spectroscopy to analyze the effect of MODCl on film formation during spin-coating.^{39,40} As presented in Fig. 3a and b, after adding chlorobenzene (CB) at 20 s, the emission peaks from the WBG films rapidly emerged. At the same time, a significant increase in the PL intensity was observed, indicating the formation of perovskite clusters in the WBG film after the removal of polar

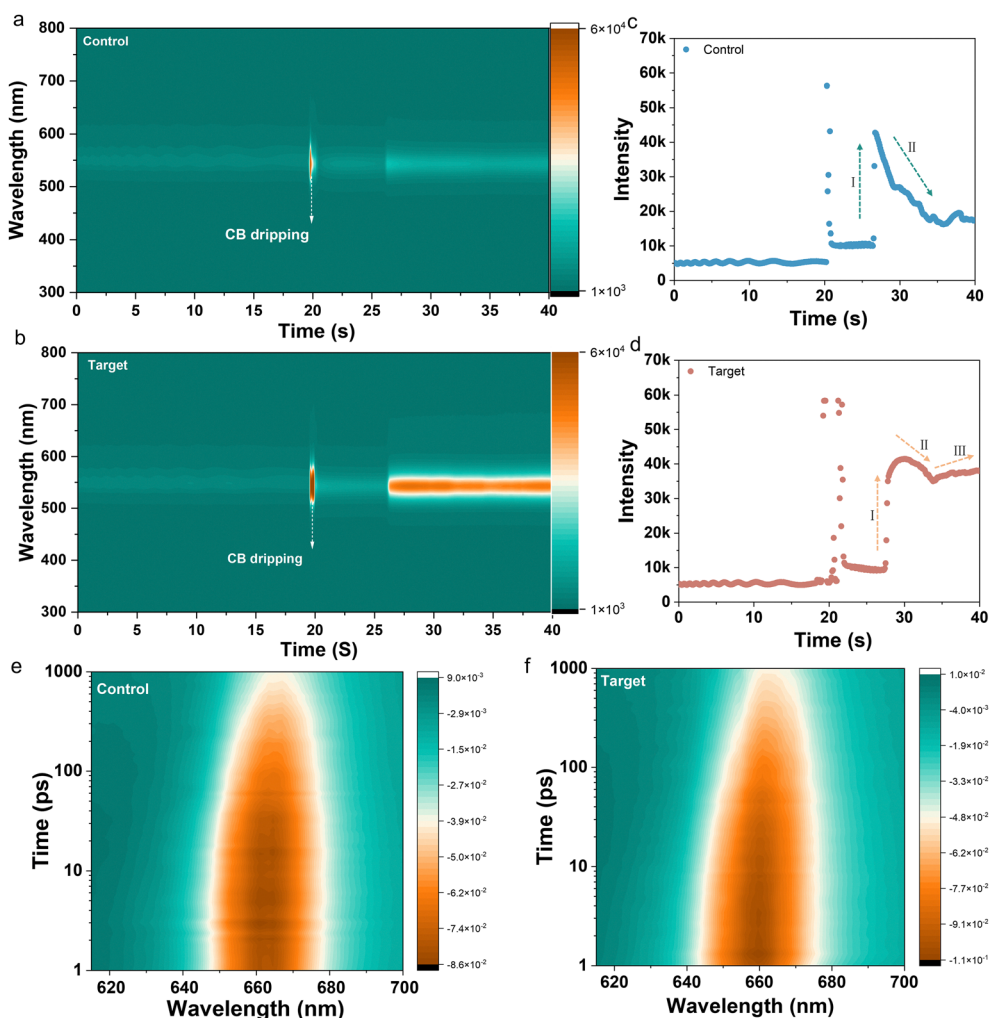


Fig. 3 *In situ* PL peak position evolution of the control (a) and target (b) WBG films. The changes in the PL intensity were extracted from 546 nm for the (c) control and (d) target WBG films. (e) and (f) Pseudo color representation of the TA results.

solvents following the addition of CB. Subsequently, a sudden drop in PL intensity was observed within the first 6 seconds, likely due to the aggregation of perovskite emitters and the development of high-density defects. The MODCl-containing target film exhibited significantly higher resistance to PL quenching compared to the control film (Fig. S10, ESI[†]), indicating that MODCl effectively suppresses defect formation during the initial crystallization process. As solvent evaporation progressed during spin-coating, the target film consistently maintained a higher PL intensity, showing a distinct advantage over the control film. The control film exhibits a typical “up-down” process, consisting of two distinct stages (Fig. 3c). In the first stage, small crystallites of perovskite continue to grow and merge, causing the film grains to increase in size, which reduces the grain boundary area and increases the PL intensity. In the second stage, the control film becomes prone to decomposition under ambient conditions, with the PL intensity declining rapidly after a brief increase. However, in the target film, the addition of MODCl introduces an extra stage, resulting in an “up-down-up” PL evolution process (Fig. 3d). The crystallization process slows significantly, reaching a maximum PL intensity at approximately 28 s and sustaining it for a longer period. This indicates that the addition of MODCl regulates crystallization kinetics, significantly improving WBG film quality, ultimately leading to larger grain sizes and higher crystallinity. During the second stage, the PL intensity decreases under the influence of environmental factors. In the additional third stage, the increase in the PL intensity is attributed to two factors: firstly, water vapor promotes grain boundary dissolution, forming larger grains; secondly, MODCl enhances perovskite crystal quality and improves WBG film stability.

Transient absorption (TA) spectroscopy was employed to investigate the spatial distribution characteristics of halide ions in perovskite films post-annealing.⁴¹ The target sample exhibited a pronounced shift in ground-state bleaching (GSA), which varied as a function of time post-excitation. At the early stage, the bleaching signal appeared at a higher energy, indicating carrier localization in Br-rich regions. Subsequently, the signal shifted to a lower energy, reflecting carrier migration toward regions with a lower Br content. Over 1000 ps, the ground-state bleaching in the target film shifted by ~ 6.42 nm, whereas the control film exhibited a shift of only ~ 3.61 nm (Fig. S11, ESI[†]). This indicates that the target film exhibits a greater Br gradient, with high-bandgap regions (higher Br content) concentrated at the film surface and low-bandgap regions (lower Br content) deeper within the film. This result indicates that the introduction of MODCl results in a halide ion gradient in the target film, forming an energy cascade structure. This structure improves solar cell stability by effectively repelling carriers away from defect-rich surfaces.^{42,43} To analyze the exciton dissociation decay, we fitted the decay curves shown in Fig. S12 (ESI[†]). The FTO/SAM/perovskite films exhibited the strongest photobleaching signal in the range of 659–666 nm. The best-fit result for the control sample indicated an exciton dissociation decay of 2124 ps. The decay for the target perovskite was determined to be 1546 ps, which is consistent with previous reports.⁴⁴

The shorter exciton dissociation decay suggests fewer defects, highlighting the superior passivation capability of MODCl.

As shown in Fig. S13 (ESI[†]), the PL test was used to verify the effect of MODCl on the phase separation of WBG perovskite films. The control film exhibited a slight red shift and clear I-rich phase under 1 sun illumination after 20 min. In contrast, the target WBG film showed only a slight red shift and didn't display the I-rich phase, indicating that MODCl enhances the phase stability of WBG perovskites by regulating halogen crystallization.

Fig. 4a shows the current–voltage (J – V) characteristics of the p–i–n type WBG PSCs, and Table S2 and Fig. S14 (ESI[†]) summarize their PV parameters. The control WBG PSC exhibited a PCE of 17.45%, with a V_{OC} of 1.353 V, a short-circuit current density (J_{SC}) of 16.19 mA cm^{-2} , and a fill factor (FF) of 79.65%, and the introduction of MODCl into the perovskite bulk phase further elevated the PCE to 18.76%, with a V_{OC} of 1.387 V, a J_{SC} of 16.06 mA cm^{-2} , and an FF of 84.20%. The increased PCE of the target device could be traceable to the largely improved V_{OC} and FF compared with the control device. Fig. 4b shows the external quantum efficiency (EQE) of the target device. The integrated current density of the target device was 15.76 mA cm^{-2} , which is in excellent agreement with the J – V results. Steady-state power output (SPO) measurements were used to verify the PCE stability of the target devices, holding the voltage at the maximum power point for 200 seconds (Fig. 4c). The average SPO PCE of the target device was 18.37%, which matches the J – V results. The capacitance–voltage (C – V) characteristics were measured using the Mott–Schottky relation (Fig. 4d), and the effect of MODCl introduction on the enhancement of V_{OC} in WBG devices was further explored. The V_{bi} values for the control and target devices were measured to be 1.10 V and 1.15 V, respectively, aligning with the observed increase in V_{OC} from the J – V curves. The enhancement of V_{bi} indicates a stronger charge transfer and collection drive, which contributes to the improvement of V_{OC} of the target WBG device.

To investigate the effectiveness of MODCl in passivating defects, we analyzed the WBG films using PL spectra (Fig. S15a, ESI[†]) and time-resolved PL decay (Fig. S15b, ESI[†]) measurements. It is evident that the intensity of the perovskite films has been significantly enhanced with the addition of MODCl, indicating that nonradiative recombination was suppressed. The TRPL data in Fig. S15b (ESI[†]) were fitted using the following biexponential function:¹⁵

$$y = A_1 \exp\left(\frac{-t}{\tau_1}\right) + A_2 \exp\left(\frac{-t}{\tau_2}\right) + y_0 \quad (1)$$

A_1 and A_2 represent the relative amplitude, and τ_1 and τ_2 correspond to the short and long decay times associated with carrier non-radiative recombination at the interface and in the bulk, respectively. The calculated average decay time (τ_{avg}) reached 1043.95 ns, nearly three times that of the control film ($\tau_{avg} = 302.51$ ns). The reduction in the grain boundaries and trap density in the target WBG film significantly suppresses carrier non-radiative recombination losses.^{45,46} A summary of the fitting data is provided in Table S3 (ESI[†]). We also conducted PL mapping to

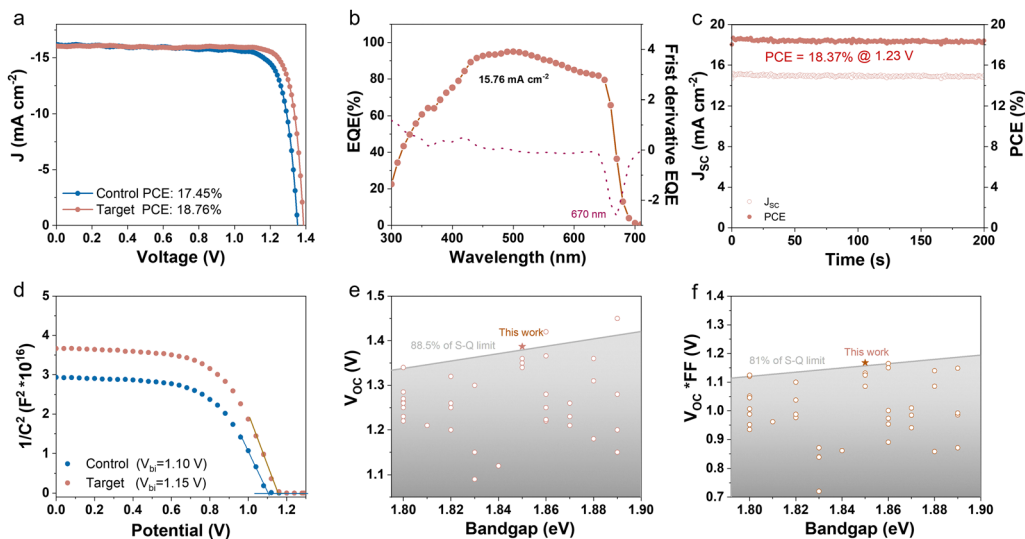


Fig. 4 (a) J - V curves of the control and target WBG PSCs. (b) The EQE spectra of the target WBG PSC. (c) The steady-state power output of the control and target WBG devices. (d) The Mott-Schottky plots for the control and target devices. (e) and (f) Comparison between the results of the champion WBG PSC device of this work and previous reports of 1.80–1.89 eV PSCs in terms of V_{OC} (e) and $V_{OC} \times FF$ (f).

get insight into the carrier quenching of perovskite films over a $2 \times 2 \mu\text{m}$ area (Fig. S16, ESI[†]), showing that the perovskite films exhibit more uniform and stronger luminescence after MODCl addition. To further investigate charge carrier recombination dynamics in whole PSCs, transient photovoltages (TPVs) were measured under simulated one-sun illumination. As shown in Fig. S17a (ESI[†]), compared with the $7.24 \mu\text{s}$ decay time of the control device, the target device possesses a longer decay time ($8.36 \mu\text{s}$), indicating that the recombination rate of charge carriers decreases, which is conducive to prolonging the carrier lifetime and diffusion length. Meanwhile, transient photocurrent (TPC) measurements were also carried out, revealing that the shorter photocurrent decay time observed in the target device might be attributed to the enhanced charge extraction capability after MODCl addition. Electrical impedance spectroscopy (EIS) was performed in the dark to investigate the charge transfer dynamics of WBG PSCs.⁴⁷ According to Fig. S18 (ESI[†]), the charge transfer resistance (R_{ct}) of the target device decreased from 281.5Ω to 117.5Ω , significantly lower than that of the control device. The lower R_{ct} in the target WBG device indicates that the charge transport efficiency is significantly enhanced after the introduction of MODCl. The defect density (N_t) was determined using the space charge limited current (SCLC) method under dark conditions. As illustrated in Fig. S19 (ESI[†]), the defect density calculated from the SCLC data decreased from $1.41 \times 10^{15} \text{ cm}^{-3}$ in the control film to $0.95 \times 10^{15} \text{ cm}^{-3}$ in the target film. The result demonstrates the effectiveness of MODCl in passivating WBG perovskites.

Additionally, the operational stability of the WBG device was studied. In comparison to the control devices, the target devices showed significantly improved operational stability, attributed to the high-quality WBG films and vertically distributed halide ions. The target device, under 1-sun illumination (white LED), retained approximately 94% of its initial efficiency after

1000 hours of maximum power point (MPP) tracking (Fig. S20, ESI[†]). By comparison, the control device's efficiency dropped by 42% within 600 hours.

To verify the reproducibility of WBG device performance, we selected 20 devices from five batches for comparison, as shown in Fig. S21 (ESI[†]). The devices doped with MODCl showed significant improvements in the PCE, V_{OC} , J_{SC} , and FF, with a narrower distribution and better reproducibility. Previous studies have shown that the $V_{OC} \times FF$ product can quantitatively analyze the V_{OC} -FF trade-off without being affected by bandgap differences.⁴⁸ The V_{OC} and $V_{OC} \times FF$ product of MODCl-doped devices reached 88.5% and 81% of the S-Q limits, respectively, making them one of the highest values reported for WBG PSCs to date (Fig. 4e and Fig. S22, ESI[†]). The previous reports of 1.80–1.89 eV WBG single-junction PSCs are summarized in Table S4 (ESI[†]). To verify the universality of MODCl, we applied it to the WBG film with $E_g = 1.80 \text{ eV}$, resulting in an improvement of the PCE from 18.48% to 19.43% and an increase in the V_{OC} from 1.328 V to 1.354 V (Table S5, ESI[†]). Significant improvements in device performance and stability, combined with an optimal bandgap (1.85 eV), make it advantageous for the application of perovskite-organic tandem solar cells (P-OTSCs).

Organic solar cells (OSCs), with advantages such as lightweight construction, ease of fabrication, broad-spectrum absorption, and compatibility with organic solvent processing, are ideal for integration with PSCs in P-OTSCs. This approach offers an efficient pathway to achieve cost-effective breakthroughs in single-junction perovskite solar cell efficiency. Leveraging these advantages, we utilized MODCl-doped WBG perovskite films to fabricate high-performance P-OTSCs. As depicted in Fig. 5a and b, the device structure consists of FTO/SAM/WBG/C60/ALD-SnOx/Au/(3,4-ethylenedioxythiophene):poly(styrenesulfonate) (Pedot:PSS)/OSC/PNDIT-F3N/Ag from the bottom to the top. The ALD-SnOx/Au/Pedot:PSS serves as the interconnecting

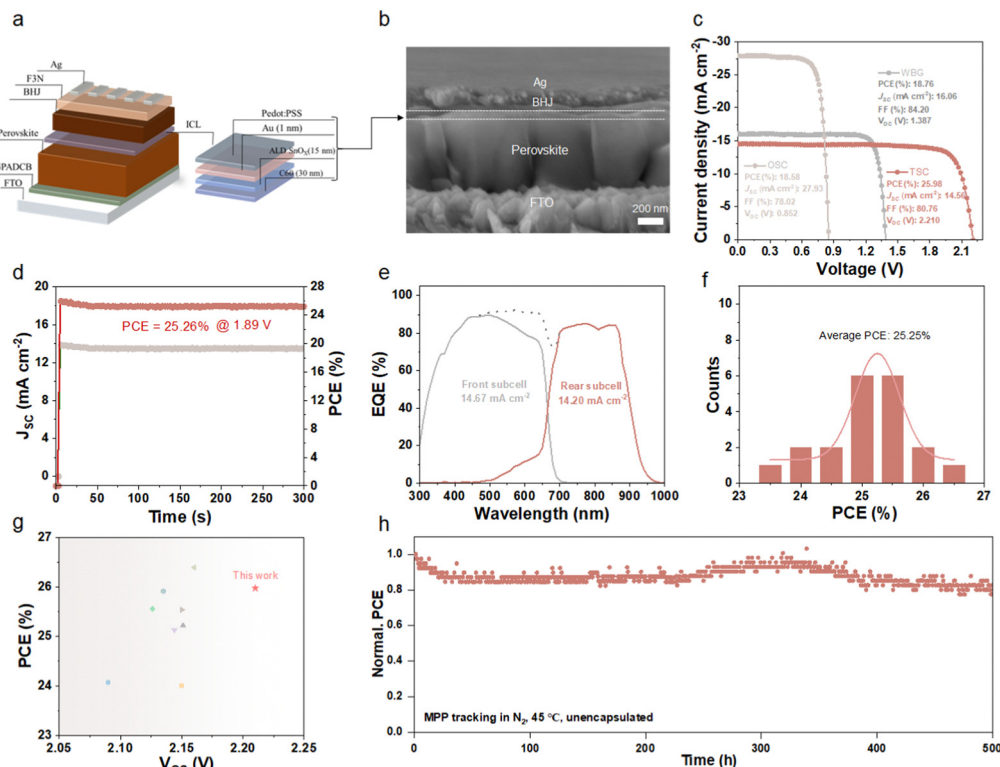


Fig. 5 (a) Schematic diagram of the P-OTSC device structure. (b) The cross-sectional SEM images of the P-OTSCs. (c) J - V curves of the WBG PSC, OSC and P-OTSCs. (d) The SPO of the P-OTSCs. (e) The EQE spectra of the P-OTSCs. (f) Statistical PCE data of the P-OTSCs. (g) Summary of reports on the performance of the P-OTSC. (h) MPP tracking of the unencapsulated P-OTSCs.

layer (ICL), while the narrow-bandgap rear sub-cell utilizes a PM6:BTP-eC9 binary blend for its bulk heterojunction (BHJ) layer. The J - V of the P-OTSC is shown in Fig. 5c, while Table S6 (ESI[†]) summarizes the photovoltaic parameters of single-junction OPVs, single-junction WBG PSCs, and P-OTSCs. The P-OTSC exhibits a PCE of 25.98%, with a V_{OC} of 2.210 V, a J_{SC} of 14.56 mA cm⁻², and an FF of 80.76%. SPO measurements were used to verify the PCE stability of the P-OTSC device, holding the voltage at the maximum power point for 300 seconds (Fig. 5d). The P-OTSC achieved an average steady-state PCE of 25.26%, which is in close agreement with the J - V results. We conducted EQE measurements on P-OTSCs, where the integrated currents of the WBG and OSC sub-cells were 14.67 mA cm⁻² and 14.20 mA cm⁻², respectively, as shown in Fig. 5e. In addition, we analyzed the PCEs of 20 P-OTSC devices from different batches, as presented in Fig. 5f. The average PCE of the P-OTSCs was 25.25%, demonstrating excellent repeatability. Notably, the V_{OC} achieved in this study represents the highest value reported for P-OTSCs (Fig. 5g and Table S7, ESI[†]), which can be attributed to the fabrication of high-quality WBG thin films. Additionally, the operational stability of the P-OTSCs was studied. The target P-OTSC device, under 1-sun illumination (white LED), retained T_{80} (the time to retain 80% of the initial efficiency) after 500 hours of MPP tracking (Fig. 5h). This strategy optimizes the crystallization dynamics of WBG perovskites, leading to the formation of high-quality WBG films, thereby enhancing the photovoltaic performance and stability of both WBG and P-OTSC devices.

Conclusion

In conclusion, our study demonstrates a successful strategy for optimizing the crystallization dynamics of WBG perovskites by incorporating MODCl into 1.85 eV I-Br mixed WBG films. The effective modulation of crystallization kinetics led to significant improvements in the film quality, effectively suppressing phase separation and enhancing the stability of WBG perovskites. The resulting WBG PSC achieved a PCE of 18.76%, with a high V_{OC} of 1.387 V and excellent operational stability. When applied to P-OTSCs, this method resulted in a PCE of 25.98% and a V_{OC} of 2.210 V, setting a new record for the highest V_{OC} reported to date. This work provides valuable insights into the crystallization kinetics of mixed halide perovskites, offering a straightforward yet highly effective strategy for fabricating stable and efficient WBG PSCs and P-OTSCs. The combination of improved crystallization dynamics and the achievement of a new V_{OC} record underscores the great promise of this approach in advancing perovskite-based photovoltaic technologies.

Author contributions

Z. S. and J. W. contributed equally to this work. Y. L., X. W., and B. X. supervised the project. Z. S. conceived the research idea and, together with J. W., designed the experimental approach. Y. B., J. Z., D. W., J. H., P. Z., B. J., Z. L., S. H., Y. H., Z. H., and C. X. contributed to the execution of experiments and

characterization. Z. S. and J. W. drafted the manuscript, while Y. C., Y. L., X. W., and B. X. refined and polished the final version. All authors reviewed and approved the manuscript.

Data availability

The data supporting this article have been included as part of the ESI.†

Conflicts of interest

The authors declare no competing financial interests.

Acknowledgements

This work was financially supported by the Shenzhen Science and Technology Innovation Committee (Grant No. SGDX20230116091649013, JCYJ20220818100211025, and KCXST2022102111616039), the Guangdong Basic and Applied Basic Research Foundation (Grant No. 2023B1515120031 and 2022A1515110413), the Natural Science Foundation of Hunan Province, China (No. 2023JJ50132), the National Natural Science Foundation of China (Grant No. 61904076, 62204108 and 62104158), the Natural Science Foundation of Top Talent of SZTU (Grant No. GDRC202113), the Project for Building a Science and Technology Innovation Center Facing South Asia and Southeast Asia (202403AP140015), and SUSTech Energy Institute for Carbon Neutrality (High level of special funds, G03034K001). We would also like to acknowledge the technical support from SUSTech Core Research Facilities and the Center for Computational Science and Engineering at SUSTech, and also the BL14B1 beamline of the Shanghai Synchrotron Radiation Facility (SSRF) for the assistance with GIWAXS measurement.

References

- J. Burschka, N. Pellet, S.-J. Moon, R. Humphry-Baker, P. Gao, M. K. Nazeeruddin and M. Grätzel, *Nature*, 2013, **499**, 316–319.
- Q. Dong, Y. Fang, Y. Shao, P. Mulligan, J. Qiu, L. Cao and J. Huang, *Science*, 2015, **347**, 967–970.
- D. Shi, V. Adinolfi, R. Comin, M. Yuan, E. Alarousu, A. Buin, Y. Chen, S. Hoogland, A. Rothenberger, K. Katsiev, Y. Losovyj, X. Zhang, P. A. Dowben, O. F. Mohammed, E. H. Sargent and O. M. Bakr, *Science*, 2015, **347**, 519–522.
- Z. Song, Y. Gao, Y. Zou, H. Zhang, R. Wang, Y. Chen, Y. Chen and Y. Liu, *J. Am. Chem. Soc.*, 2024, **146**, 1657–1666.
- N. Chen, T. Cai, W. Li, K. Hills-Kimball, H. Yang, M. Que, Y. Nagaoka, Z. Liu, D. Yang and A. Dong, *ACS Appl. Mater. Interfaces*, 2019, **11**, 16855–16863.
- A. Kojima, K. Teshima, Y. Shirai and T. Miyasaka, *J. Am. Chem. Soc.*, 2009, **131**, 6050–6051.
- N. r. e. laboratory, best research-cell efficiency chart, <https://www.nrel.gov/pv/cell-efficiency.html>, (accessed December, 2024).
- X. Li, Y. Li, Y. Feng, J. Qi, J. Shen, G. Shi, S. Yang, M. Yuan and T. He, *Adv. Mater.*, 2024, **36**, 2401103.
- W. Shockley and H. J. Queisser, *J. Appl. Phys.*, 1961, **32**, 510–519.
- H. Lin, M. Yang, X. Ru, G. Wang, S. Yin, F. Peng, C. Hong, M. Qu, J. Lu, L. Fang, C. Han, P. Procel, O. Isabella, P. Gao, Z. Li and X. Xu, *Nat. Energy*, 2023, **8**, 789–799.
- L. Zhu, M. Zhang, J. Xu, C. Li, J. Yan, G. Zhou, W. Zhong, T. Hao, J. Song, X. Xue, Z. Zhou, R. Zeng, H. Zhu, C.-C. Chen, R. C. I. MacKenzie, Y. Zou, J. Nelson, Y. Zhang, Y. Sun and F. Liu, *Nat. Mater.*, 2022, **21**, 656–663.
- D. Wang, M. Chen, X. Lei, Y. Wang, Y. Bao, X. Huang, P. Zhu, J. Zeng, X. Wang, S. Tsang, F. Li, B. Xu and A. K.-Y. Jen, *Adv. Mater.*, 2024, **36**, 2411677.
- B. Zhao, M. Abdi-Jalebi, M. Tabachnyk, H. Glass, V. S. Kamboj, W. Nie, A. J. Pearson, Y. Puttisong, K. C. Gödel, H. E. Beere, D. A. Ritchie, A. D. Mohite, S. E. Dutton, R. H. Friend and A. Sadhanala, *Adv. Mater.*, 2017, **29**, 1604744.
- L. Protesescu, S. Yakunin, M. I. Bodnarchuk, F. Krieg, R. Caputo, C. H. Hendon, R. X. Yang, A. Walsh and M. V. Kovalenko, *Nano Lett.*, 2015, **15**, 3692–3696.
- Z. Song, J. Yang, X. Dong, R. Wang, Y. Dong, D. Liu and Y. Liu, *Nano Lett.*, 2023, **23**, 6705–6712.
- X. Guo, Z. Jia, S. Liu, R. Guo, F. Jiang, Y. Shi, Z. Dong, R. Luo, Y.-D. Wang, Z. Shi, J. Li, J. Chen, L. K. Lee, P. Müller-Buschbaum, D. S. Ginger, D. J. Paterson and Y. Hou, *Joule*, 2024, **8**, 2554–2569.
- Y. An, N. Zhang, Z. Zeng, Y. Cai, W. Jiang, F. Qi, L. Ke, F. R. Lin, S.-W. Tsang, T. Shi, A. K.-Y. Jen and H.-L. Yip, *Adv. Mater.*, 2024, **36**, 2306568.
- Y. Zheng, X. Wu, J. Liang, Z. Zhang, J. Jiang, J. Wang, Y. Huang, C. Tian, L. Wang, Z. Chen and C.-C. Chen, *Adv. Funct. Mater.*, 2022, **32**, 2200431.
- F. Peña-Camargo, P. Caprioglio, F. Zu, E. Gutierrez-Partida, C. M. Wolff, K. Brinkmann, S. Albrecht, T. Riedl, N. Koch, D. Neher and M. Stollerfoht, *ACS Energy Lett.*, 2020, **5**, 2728–2736.
- E. T. Hoke, D. J. Slotcavage, E. R. Dohner, A. R. Bowring, H. I. Karunadasa and M. D. McGehee, *Chem. Sci.*, 2015, **6**, 613–617.
- J. Tong, Q. Jiang, F. Zhang, S. B. Kang, D. H. Kim and K. Zhu, *ACS Energy Lett.*, 2021, **6**, 232–248.
- F. Xu, M. Zhang, Z. Li, X. Yang and R. Zhu, *Adv. Energy Mater.*, 2023, **13**, 2203911.
- S. Mahesh, J. M. Ball, R. D. J. Oliver, D. P. McMeekin, P. K. Nayak, M. B. Johnston and H. J. Snaith, *Energy Environ. Sci.*, 2020, **13**, 258–267.
- C. Yang, D. Liu, M. Bates, M. C. Barr and R. R. Lunt, *Joule*, 2019, **3**, 1803–1809.
- Y. C. Kim, H. J. An, D. H. Kim, J.-M. Myoung, Y. J. Heo and J. H. Cho, *Adv. Funct. Mater.*, 2021, **31**, 2005553.
- X. Shen, B. M. Gallant, P. Holzhay, J. A. Smith, K. A. Elmetekawy, Z. Yuan, P. V. G. M. Rathnayake, S. Bernardi, A. Dasgupta, E. Kasparavicius, T. Malinauskas, P. Caprioglio, O. Shargaieva, Y.-H. Lin, M. M. McCarthy,

- E. Unger, V. Getautis, A. Widmer-Cooper, L. M. Herz and H. J. Snaith, *Adv. Mater.*, 2023, **35**, 2211742.
- 27 Z. Zhang, W. Chen, X. Jiang, J. Cao, H. Yang, H. Chen, F. Yang, Y. Shen, H. Yang, Q. Cheng, X. Chen, X. Tang, S. Kang, X.-m Ou, C. J. Brabec, Y. Li and Y. Li, *Nat. Energy*, 2024, **9**, 592–601.
- 28 C. Chen, Y. Kuang, S. Zhu, I. Burgert, T. Keplinger, A. Gong, T. Li, L. Berglund, S. J. Eichhorn and L. Hu, *Nat. Rev. Mater.*, 2020, **5**, 642–666.
- 29 Z. Zhang, J. Wang, J. Liang, Y. Zheng, X. Wu, C. Tian, A. Sun, Y. Huang, Z. Zhou, Y. Yang, Y. Liu, C. Tang, Z. Chen and C.-C. Chen, *Small*, 2023, **19**, 2303213.
- 30 A. S. Subbiah, S. Mannar, V. Hnapovskiy, A. R. Pininti, B. Vishal, L. V. Torres Merino, O. Matiash, O. Karalis, H. Hempel, A. Prasetyo, B. Yildirim, P. Dally, D. Rosas Villalva, M. Babics, L. Xu, A. Razzaq, R. Azmi, F. Xu, H. L. Bristow, E. Ugur, A. Ur Rehman, H. Pasanen, E. Aydin, T. Allen, D. Baran, T. Unold, F. Laquai and S. De Wolf, *Joule*, 2025, **9**, 101767.
- 31 M. Yang, Y. Bai, Y. Meng, R. Tian, K. Sun, X. Lu, H. Pan, J. Wang, S. Zhou, J. Zhang, Z. Song, Y. Wang, C. Liu and Z. Ge, *Adv. Mater.*, 2024, **37**, 2415627.
- 32 B. Ding, Y. Ding, J. Peng, J. Romano-deGea, L. E. K. Frederiksen, H. Kanda, O. A. Syzgantseva, M. A. Syzgantseva, J.-N. Audinot, J. Bour, S. Zhang, T. Wirtz, Z. Fei, P. Dörflinger, N. Shibayama, Y. Niu, S. Hu, S. Zhang, F. F. Tirani, Y. Liu, G.-J. Yang, K. Brooks, L. Hu, S. Kinge, V. Dyakonov, X. Zhang, S. Dai, P. J. Dyson and M. K. Nazeeruddin, *Nature*, 2024, **628**, 299–305.
- 33 F. Li, X. Deng, Z. Shi, S. Wu, Z. Zeng, D. Wang, Y. Li, F. Qi, Z. Zhang, Z. Yang, S.-H. Jang, F. R. Lin, S. W. Tsang, X.-K. Chen and A. K. Y. Jen, *Nat. Photonics*, 2023, **17**, 478–484.
- 34 M. Saliba, T. Matsui, K. Domanski, J.-Y. Seo, A. Ummadisingu, S. M. Zakeeruddin, J.-P. Correa-Baena, W. R. Tress, A. Abate, A. Hagfeldt and M. Grätzel, *Science*, 2016, **354**, 206–209.
- 35 D. Bi, C. Yi, J. Luo, J.-D. Décoppet, F. Zhang, S. M. Zakeeruddin, X. Li, A. Hagfeldt and M. Grätzel, *Nat. Energy*, 2016, **1**, 16142.
- 36 Y. Gao, Z. Song, Q. Fu, Y. Chen, L. Yang, Z. Hu, Y. Chen and Y. Liu, *Adv. Mater.*, 2024, **36**, 2405921.
- 37 R. Azmi, E. Ugur, A. Seitkhan, F. Aljamaan, A. S. Subbiah, J. Liu, G. T. Harrison, M. I. Nugraha, M. K. Eswaran, M. Babics, Y. Chen, F. Xu, T. G. Allen, A. U. Rehman, C.-L. Wang, T. D. Anthopoulos, U. Schwingenschlögl, M. De Bastiani, E. Aydin and S. De Wolf, *Science*, 2022, **376**, 73–77.
- 38 H. Wang, C. Zhu, L. Liu, S. Ma, P. Liu, J. Wu, C. Shi, Q. Du, Y. Hao, S. Xiang, H. Chen, P. Chen, Y. Bai, H. Zhou, Y. Li and Q. Chen, *Adv. Mater.*, 2019, **31**, 1904408.
- 39 N. Mrkyvkova, V. Held, P. Nádaždy, R. Subair, E. Majkova, M. Jergel, A. Vlk, M. Ledinsky, M. Kotlár, J. Tian and P. Siffalovic, *J. Phys. Chem. Lett.*, 2021, **12**, 10156–10162.
- 40 T.-B. Song, Z. Yuan, M. Mori, F. Motiwala, G. Segev, E. Masquelier, C. V. Stan, J. L. Slack, N. Tamura and C. M. Sutter-Fella, *Adv. Funct. Mater.*, 2020, **30**, 1908337.
- 41 Q. Jiang, J. Tong, R. A. Scheidt, X. Wang, A. E. Louks, Y. Xian, R. Tirawat, A. F. Palmstrom, M. P. Hautzinger, S. P. Harvey, S. Johnston, L. T. Schelhas, B. W. Larson, E. L. Warren, M. C. Beard, J. J. Berry, Y. Yan and K. Zhu, *Science*, 2022, **378**, 1295–1300.
- 42 Z. Yu, X. Chen, S. P. Harvey, Z. Ni, B. Chen, S. Chen, C. Yao, X. Xiao, S. Xu, G. Yang, Y. Yan, J. J. Berry, M. C. Beard and J. Huang, *Adv. Mater.*, 2022, **34**, 2110351.
- 43 Q. Zhao, A. Hazarika, X. Chen, S. P. Harvey, B. W. Larson, G. R. Teeter, J. Liu, T. Song, C. Xiao, L. Shaw, M. Zhang, G. Li, M. C. Beard and J. M. Luther, *Nat. Commun.*, 2019, **10**, 2842.
- 44 C.-M. Hung, C.-L. Mai, C.-C. Wu, B.-H. Chen, C.-H. Lu, C.-C. Chu, M.-C. Wang, S.-D. Yang, H.-C. Chen, C.-Y. Yeh and P.-T. Chou, *Angew. Chem., Int. Ed.*, 2023, **62**, e202309831.
- 45 C. Luo, G. Zheng, F. Gao, X. Wang, Y. Zhao, X. Gao and Q. Zhao, *Joule*, 2022, **6**, 240–257.
- 46 C. Luo, W. Li, J. Fu and W. Yang, *Chem. Mater.*, 2019, **31**, 5616–5624.
- 47 W. Chen, Y. Z. Wu, Y. F. Yue, J. Liu, W. J. Zhang, X. D. Yang, H. Chen, E. B. Bi, I. Ashraful, M. Grätzel and L. Y. Han, *Science*, 2015, **350**, 944–948.
- 48 W. Peng, K. Mao, F. Cai, H. Meng, Z. Zhu, T. Li, S. Yuan, Z. Xu, X. Feng, J. Xu, M. D. McGehee and J. Xu, *Science*, 2023, **379**, 683–690.